

# Evaluating INS/GNSS Availability for Self-Driving Cars in Urban Environments

Kana Nagai, Matthew Spenko, Ron Henderson, Boris Pervan, *Illinois Institute of Technology*

## BIOGRAPHY

**Kana Nagai** obtained her B.S. in Mechanical Engineering from Illinois Institute of Technology (IIT), and B.E. in Architecture from Hokkaido University, Japan. She is currently a Ph.D. candidate and Research Assistant in Mechanical and Aerospace Engineering at IIT.

**Matthew Spenko** is a Professor of Mechanical and Aerospace Engineering at the Illinois Institute of Technology. He earned his B.S. degree in Mechanical Engineering from Northwestern University in 1999 and M.S. and Ph.D. degrees in Mechanical Engineering from the Massachusetts Institute of Technology in 2001 and 2005, respectively. From 2005–2007 he was an Intelligence Community postdoctoral fellow working at Stanford University in the Mechanical Engineering Department.

**Ron Henderson FASLA** is Professor and Director of the Landscape Architecture + Urbanism Program at Illinois Institute of Technology. He is founding principal of LIRIO Landscape Architecture, Senior Fellow at Dumbarton Oaks, and a Japan-US Creative Fellow. Prof. Henderson received his B.Arch. from University of Notre Dame and his Master of Landscape Architecture and Master of Architecture from University of Pennsylvania.

**Boris Pervan** is a Professor of Mechanical and Aerospace Engineering at IIT, where he conducts research on advanced navigation systems. Prior to joining the faculty at IIT, he was a spacecraft mission analyst at Hughes Aircraft Company (now Boeing) and a postdoctoral research associate at Stanford University. Prof. Pervan received his B.S. from the University of Notre Dame, M.S. from the California Institute of Technology, and Ph.D. from Stanford University.

## ABSTRACT

We evaluate fault-free integrity of tightly coupled INS/GNSS-based navigation for a self-driving car in a dense urban environment. Specifically, we estimate how long and under what local conditions a vehicle's navigation protection level does not exceed an alert limit in a real urban environment—in our case, 3D-mapped downtown Chicago. We use a practical integrated navigation system, consisting of GNSS, INS, wheel speed sensors, and vehicle dynamic constraints. The goal is to determine at what locations augmentation from external ranging sources is needed to maintain continuous navigation with fault-free integrity. The results show that the vehicle velocity passing through GPS-denied areas strongly affects INS/GPS performance, and that wheel speed sensors and vehicle dynamic constraints can provide some relief.

## I. INTRODUCTION

GNSS provides navigation services globally, but satellite visibility in urban areas is limited by high-rise buildings. This creates a mixture of GNSS available and denied environments (Fig. 1), and users do not generally know where the system can maintain sufficient levels accuracy and integrity for a particular application. To begin to address the issue for self-driving cars, we evaluated GNSS-only availability in downtown Chicago in [1].

GNSS signal prediction in urban environments has been conducted in previous work. For example, the concept of “shadow matching” [2] was developed to identify GNSS signal blockages in urban canyons. Overlaying sky plots on a hemispherical sky view can be used to distinguish between line of sight (LOS) and non-line of sight (NLOS) signals (Fig. 2a) [3]. Reflected rays can be predicted using Householder transformations [4] to reveal potential multipath conditions. Satellites producing blocked or reflected NLOS signals should be excluded to maintain integrity.

When the number of visible satellites is greater than three, GNSS can resolve vehicle position. However, even in cases where enough satellites are visible, the satellite geometries are generally weak because the dilution of precision (DOP) is adversely affected by the buildings partially occupying the sky. Horizontal positioning error must be bounded by a protection level computed by the vehicle. Then, for navigation to be deemed ‘available,’ the protection level must not exceed a required alert limit (Fig. 2b) [5]. The maximum allowed probability of exceedance (Fig. 2c) and the alert limit can together be used to determine the maximum allowable position error standard deviation.

Even if the protection level is far below the alert limit in an open sky environment, it will frequently exceed the alert limit once the vehicle enters a city. GNSS alone is generally not able to maintain availability, so integration with other sensors is

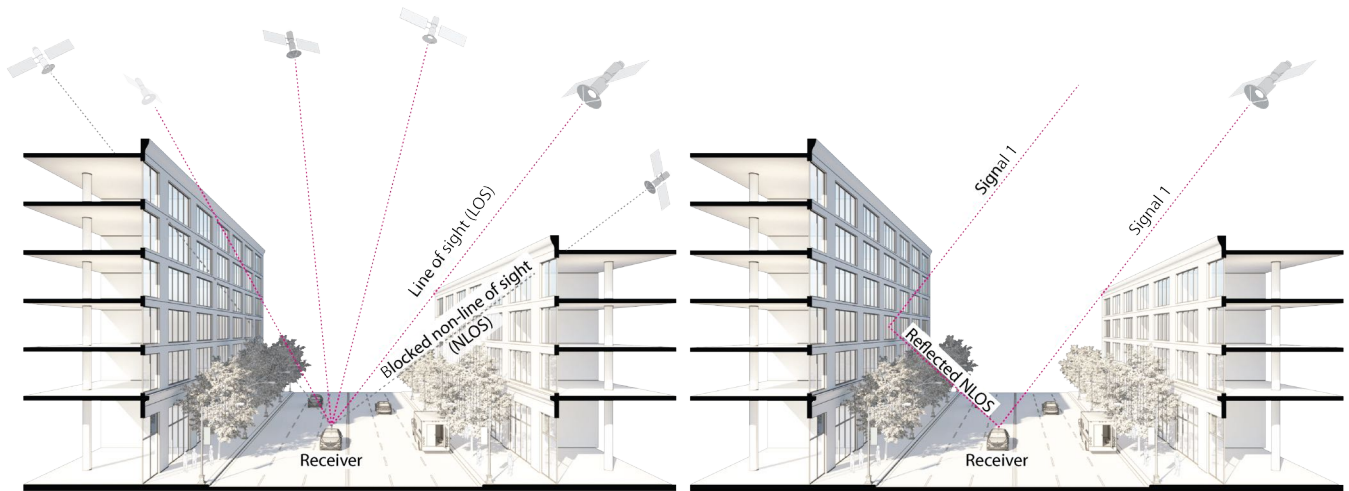


**Figure 1:** The figure depicts three types of GNSS signal reception: direct LOS signals and blocked NLOS signals (left) and reflected NLOS signals (right).

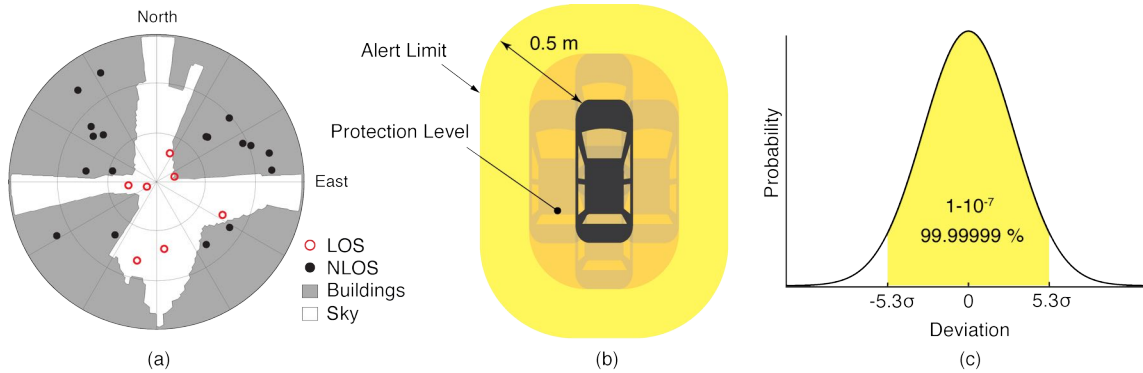


**Figure 2:** (a) A hemispherical sky view in an urban environment. (b) Illustration of a protection level and an alert limit. To ensure integrity, the protection level must not exceed an alert limit. (c) The allowable probability of exceedance is assumed to be  $10^{-7}$  in this work.

needed. Tightly coupled INS/GNSS using the Extended Kalman filter (EKF) provides better estimation in urban environments [6]. The EKF algorithm also enables integration of wheel speed sensors and vehicle dynamic constraints [7]. These integrated navigation systems will improve availability, but it is still unclear how long such a system can be expected to maintain fault-free integrity in a congested city.

Focusing on the problem of self-driving cars in urban environments, we evaluate protection levels of navigation with practical integrated sensors: GNSS, inertial navigation system (INS), wheel speed sensor (WSS), and vehicle dynamic constraint (VDC). The goal is to develop the means by which we can determine locations where external ranging sources (e.g., Lidar) are needed to maintain continuous navigation with fault-free integrity.

The remainder of this paper is laid out as follows. Section II evaluates GNSS-only availability in 3D-mapped downtown Chicago. Section III presents multi-sensor integrated navigation systems developed from tightly coupled INS/GNSS using the EKF. We introduce the measurement models and test the error growth of each system in GNSS-denied environments. Section IV proposes a simulation scenario in which the multi-sensor systems could be used. Section V discusses the initialization and alignment process for self-driving cars. In Section VI, we execute the simulations to know how long and under what local conditions multi-sensor systems can maintain fault-free integrity in a real urban environment (downtown Chicago). Finally, Section VII presents our conclusions.

## II. GNSS-ONLY AVAILABILITY

For GNSS availability evaluation, we assume an integrity requirement that the probability exceeding a 0.5-meter alert limit must be lower than  $10^{-7}$ . The 0.5-meter alert limit therefore corresponds to approximately  $5\sigma_{\text{pos}}$ , so the maximum allowable position

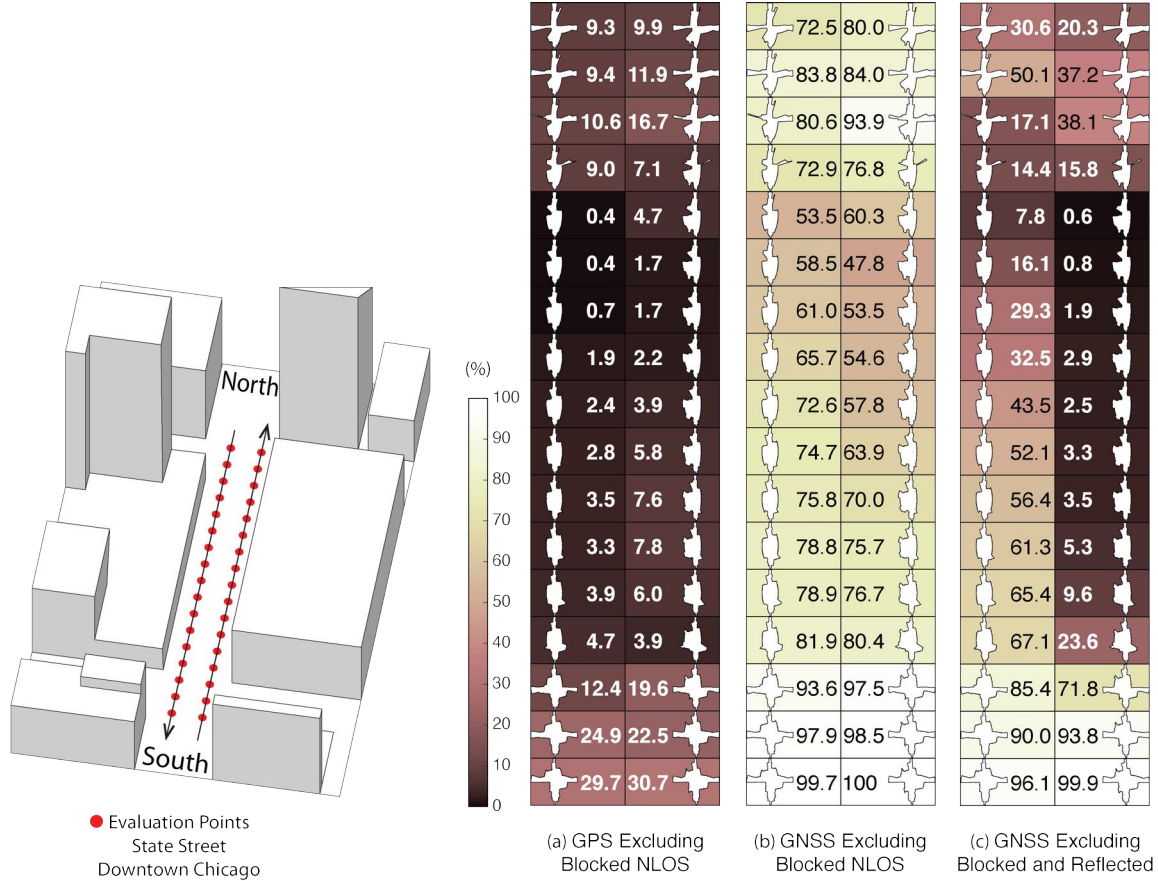


**Figure 3:** The percentage of GPS or GNSS availability in the 3-D mapped downtown Chicago. We exclude satellites producing blocked NLOS signals or both blocked and reflected NLOS signals from the measurement. Each column expresses a lane of southbound or northbound. The availability is the percentage of total time when HDOP meets the self-driving car integrity requirements in 24 hours.

error standard deviation ( $\sigma_{\text{pos}}$ ) is then approximately 0.1 meters. Accuracy at this level clearly requires differential GNSS carrier phase. We assume a nominal GNSS double difference (DD) carrier ranging error standard deviation ( $\sigma_{\text{user}}$ ) of approximately 0.02 meters, and that carrier cycle ambiguities can be readily resolved in an open sky environment prior to initiation of vehicle motion. The horizontal DOP (HDOP) is defined as

$$\sigma_{\text{pos}} = \sigma_{\text{user}} \cdot \text{HDOP}. \quad (1)$$

Given the assumptions made just above of the maximum allowable position error standard deviation and the GNSS ranging error standard deviation, the the maximum allowable HDOP is about 5.

Fig. 3 shows GPS and GNSS availability—i.e., the fraction of time the HDOP requirement is met over 24 hours—along a section of State Street in downtown Chicago. The availability results using GPS only and excluding only blocked NLOS signals ranged from 0% to 9% along the block and 9% to 30% at the intersections (Fig. 3a). Using four full GNSS constellations, GPS, Galileo, GLONASS, and BeiDou, availability ranged from 48% to 82% along the block and 72% to 100% at the intersections (Fig. 3b). When we also excluded satellites producing reflected NLOS signals that reach the vehicle, the availability dropped significantly at every point (Fig. 3c). We assert that Fig. 3c expresses the reality of GNSS availability because building-reflected multipath signals degrade positioning accuracy and would affect integrity negatively. It's obvious from these results that GNSS alone is insufficient to meet the autonomous driving requirements in an urban environment, and multi-sensor integrated navigation systems are needed to augment poor GNSS signal availability.

### III. MULTI-SENSOR INTEGRATION

We begin by considering tightly coupled GNSS/INS integration using an EKF and then integrate a realistic sensor suite including wheel speed sensors and vehicle dynamic constraints that enforce resistance to lateral sliding and vertical movement. If it is known from *another* source that the vehicle is not moving (e.g., it is in parking gear), a static mode constraint (SMC) can also be applied.

#### 1. Tightly Coupled INS/GNSS Integration

Tightly coupled INS/GNSS integration with an EKF [8] utilizes the INS measurement to predict the vehicle motion. The continuous process model is described as

$$\dot{\mathbf{x}}_k = \mathbf{F}_k \mathbf{x}_k + \mathbf{G}_{uk} \mathbf{u}_k + \mathbf{G}_{wk} \mathbf{w}_k \quad (2)$$

where  $\mathbf{x} = [\delta \mathbf{r}_N, \delta \mathbf{v}_N, \delta \mathbf{E}_N, \mathbf{b}, \mathbf{N}]^T$  is the state vector having position  $\mathbf{r}$  in the navigation frame, velocity  $\mathbf{v}$ , attitude  $\mathbf{E}$ , bias errors  $\mathbf{b}$ , and cycle ambiguities  $\mathbf{N}$ .  $\mathbf{u} = [\delta \tilde{\mathbf{f}}_B, \delta \tilde{\boldsymbol{\omega}}_B]^T$  is the input vector having accelerometer specific force measurement  $\tilde{\mathbf{f}}$  in the body frame, and gyro rotation rate measurement  $\tilde{\boldsymbol{\omega}}$ .  $\mathbf{w} \sim (0, \mathbf{W})$  is a white noise vector driving the IMU states.

The GPS/GNSS measurement model is

$$\mathbf{z}_k = \mathbf{H}_k \mathbf{x}_k + \mathbf{\Gamma}_{vk} \mathbf{v}_k \quad (3)$$

where  $\mathbf{z}$  is the measurement vector having carrier and code phases, and  $\mathbf{H}$  is the observation matrix containing line of sight vectors.  $\mathbf{v} \sim (0, \mathbf{V})$  is the vector of white receiver thermal noise.

#### 2. INS/GNSS/WSS/VDC Integration

For the vehicle in motion, we develop a model consisting of a wheel speed sensor measurement in the along-track direction ( $v_x$ ), non-holonomic constraint resisting lateral sliding ( $v_y$ ), and holonomic constraint on vertical movement ( $v_z$ ) (Fig. 4).

$$\begin{aligned} \boldsymbol{\omega} - \boldsymbol{\omega}^* = & {}^B \mathbf{R}^{N*} \delta \mathbf{v}_N + ({}^B \mathbf{R}^{N*} \mathbf{v}_N^* \times + \mathbf{L}_B {}^B \mathbf{R}^{N*} \mathbf{I} \boldsymbol{\omega}_N^E \times) \delta \mathbf{E}_N + \mathbf{L}_B \mathbf{b}_g \\ & + \begin{bmatrix} -\frac{\omega_R}{2} \delta r_R - \frac{\omega_L}{2} \delta r_L \\ 0 \\ 0 \end{bmatrix} - \mathbf{L}_B \delta^I \tilde{\boldsymbol{\omega}}_B^B + [\mathbf{L}_B \quad \mathbf{I}] \mathbf{v}_\omega \end{aligned} \quad (4)$$

where  $\boldsymbol{\omega} = [(\omega_R r_0 + \omega_L r_0)/2, 0, 0]^T$  is the measurement vector of velocity obtained from the wheel speed sensors and vehicle dynamic constraints. The derivation of this measurement equation is given in the appendix. The INS/GNSS/WSS/VDC integration using the EKF consists of the process model (2) and the measurement models (3), (4).

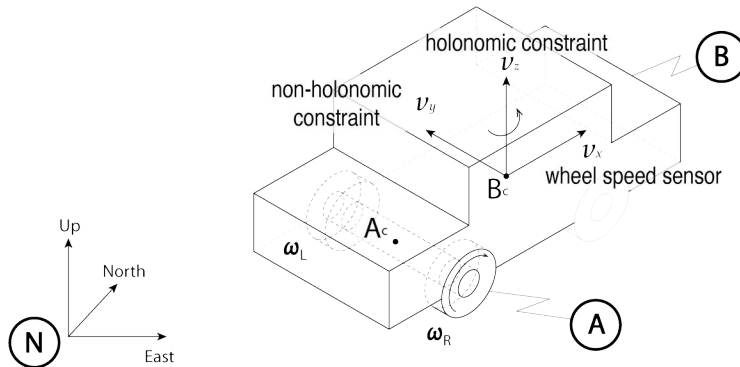


**Figure 4:** The measurement model consisting of the wheel speed sensor measurement in the along-track direction ( $v_x$ ), non-holonomic constraint resisting lateral sliding ( $v_y$ ), and holonomic constraint on vertical movement ( $v_z$ ).

#### 3. INS/GNSS/SMC Integration

The static mode constraint provides zero-velocity measurements to the EKF measurement update to mitigate position error propagation. We use SMC only when it is known that the vehicle is not moving; for example, when the vehicle is in parking

gear. The velocity in the body frame is

$$\mathbf{v}_B = {}^B \mathbf{R}^N \mathbf{v}_N \quad (5)$$

where  ${}^B \mathbf{R}^N$  is a rotation matrix from the navigation to the body frame. When equation (5) is linearized and expressed in perturbation form, we obtain the measurement vector for SMC,

$$\delta \mathbf{v}_B = {}^B \mathbf{R}^{N*} \delta \mathbf{v}_N + \mathbf{v}_B^* \times \delta \mathbf{E}_N + \zeta \quad (6)$$

with  $\delta \mathbf{v}_B = 0$ .  $\zeta$  is the white noise vector added to capture nominal (small movement) constraint violations.

#### 4. Error Propagation Analysis

We test the time from perfect initialization when position error exceeds 0.1 meters in GNSS-denied environments. Fig. 4 shows the error growth in the along-track ( $x$ ), the cross-track ( $y$ ), and the vertical ( $z$ ). The error specifications for a STIM300 tactical grade IMU are used in this analysis. The standard deviation of the wheel speed sensor measurement noise is assumed to be 0.05 m/s [7], and the standard deviation of the movement constraint violations is 0.001 m/s. The vehicle is moving at 5 m/s except when we test the SMC.

The INS can coast 15.6 seconds before the position error standard deviation exceeds 0.1 meters in both the along-track and the cross-track directions (Fig. 5a). The INS/WSS/VDC can coast 16.5 seconds in the along-track, and well over 40 seconds (the simulation duration) in the cross-track (Fig. 5b). In static mode, INS/SMC estimate errors do not grow with time in any direction, as expected (Fig. 5c). In GNSS-denied environments, the non-holonomic constraint suppresses the cross-track position error, but the wheel speed sensor measurement hardly affects the along-track position error. The SMC works perfectly, but the usage is limited to when the vehicle is known to be stationary.

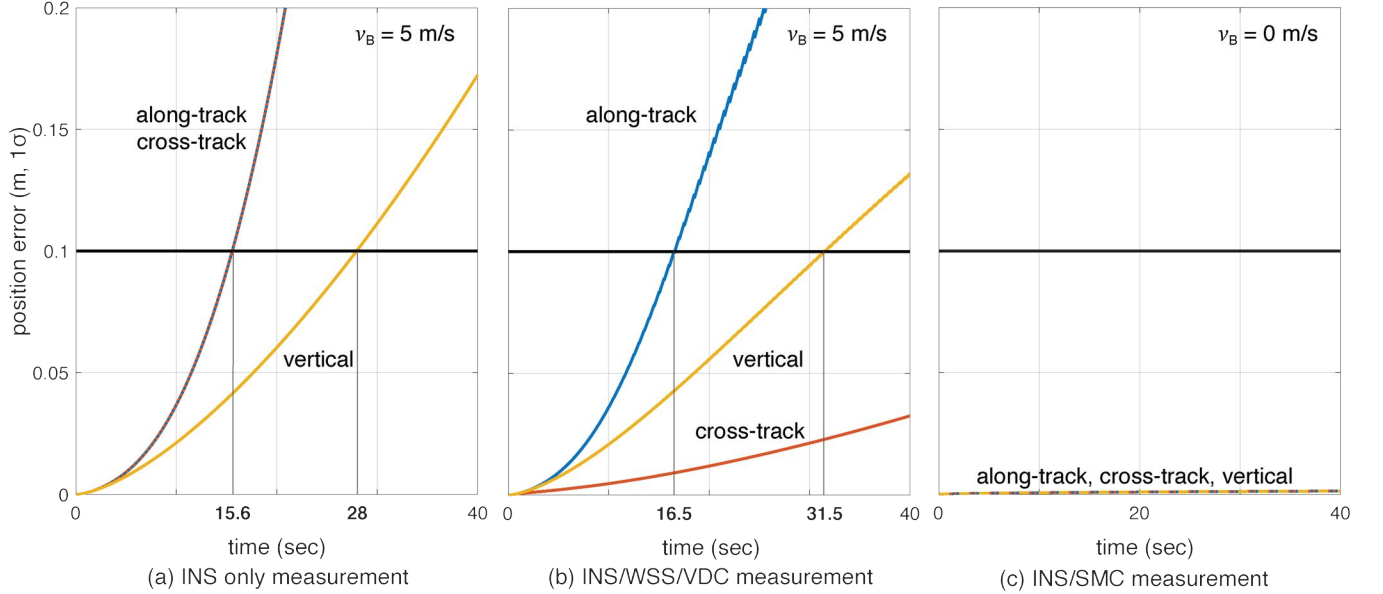


**Figure 5:** The vehicle position error growth vs. time in the along-track ( $x$ ), cross-track ( $y$ ), and vertical ( $z$ ) directions. Each graph represents the navigation system introduced in Section III. The vehicle is moving at 5 m/s (a) (b) or 0 m/s (c).

#### IV. SIMULATION SCENARIO

We imagine a future driverless car mission scenario in which multi-sensor navigation systems are practicable. To minimize congestion in a city, autonomous vehicles will be held outside the urban core when not in use. In the clear open-sky environment, a vehicle in parking lot completes GNSS initialization using the INS/GNSS/SMC system. Once requested for action, the vehicle departs for the city from the parking lot, and the motion of the vehicle improves alignment by the INS/GNSS system. Safe navigation can be ensured using the system to provide continuity under overpasses and bridges in the open-sky environment. Upon entering the urban core, navigation becomes more dependent on the INS/WSS/VDC system.

Recall, we assume an integrity requirement in which the probability of exceeding a 0.5-meter alert limit must be lower than

$10^{-7}$ , and the maximum allowable position error standard deviation becomes 0.1 meters. A reasonable numerical target for differential GNSS initialized position error is 0.02 meters, and for the INS alignment yaw angle error 0.1 degrees.

Local GNSS multipath errors due to nearby vehicles will vary with the satellite elevation angle. Prior experimental results show lower elevation satellite signals (below 33 degrees) are much more likely to be impacted by multipath than higher ones [9]. Multipath is a time correlated error that we model as a first-order Gauss Markov process. We use different error model parameters above and below 33 degrees as presented in Table 1.

**Table 1:** The nominal GNSS multipath error values in the simulation [9].

Elevation Angle (degrees)	Carrier Phase		Code Phase	
	$\sigma_\phi$ (m)	$\tau_\phi$ (sec)	$\sigma_\rho$ (m)	$\tau_\rho$ (sec)
$\epsilon \leq 33$	0.027	150	1.38	80
$\epsilon > 33$	0.0077	150	0.62	80

## V. INITIALIZATION AND ALIGNMENT

Initialization takes place in a parking lot with a clear sky view. A vehicle is in park, enabling SMC to be applied. We consider initialization to be complete when the horizontal position error standard deviation reaches 0.02 m. Fig. 6a) shows a typical example, showing that with INS/GPS/SMC initialization system takes about 31 minutes and with INS/GPS only about 36 minutes. SMC does speed up GPS initialization, although the improvement is modest.

The yaw angle is not aligned during the initialization, but roll and pitch are immediately aligned (Fig. 6b). Earth’s gravity affects roll and pitch angle alignment but not yaw angle.

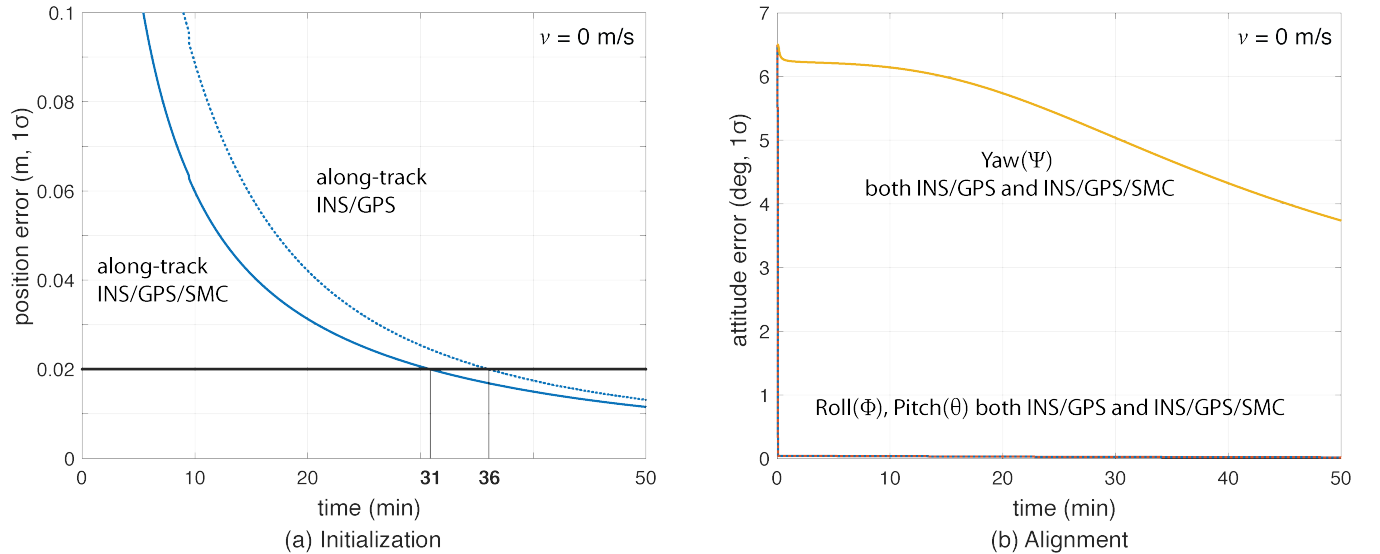


**Figure 6:** (a) Comparisons of initialization time between INS/GPS and INS/GPS/SMC in an open-sky environment. The INS/GPS/SMC system initializes rapidly. (b) Transitions of roll, pitch, yaw alignment during the initialization. Yaw angle alignment cannot be performed when the vehicle is stationary.

Yaw angle alignment cannot be performed when the vehicle is stationary or moving with constant velocity. Accelerated motion, either straight or turning, is required. Fig. 7 shows the behavior of the yaw angle error standard deviation using the INS/GPS system when centripetal (Fig. 7a) or tangential (Fig. 7b) acceleration is applied. The yaw angle can be aligned in a couple of seconds either type of acceleration. To represent typical initial motions of self-driving cars, we model a parking lot departure via a “Z” shaped path (i.e., two turns) with stop signs at each turn. In this scenario, the yaw alignment error reaches 0.1 degrees within a couple of seconds (Fig. 7c).

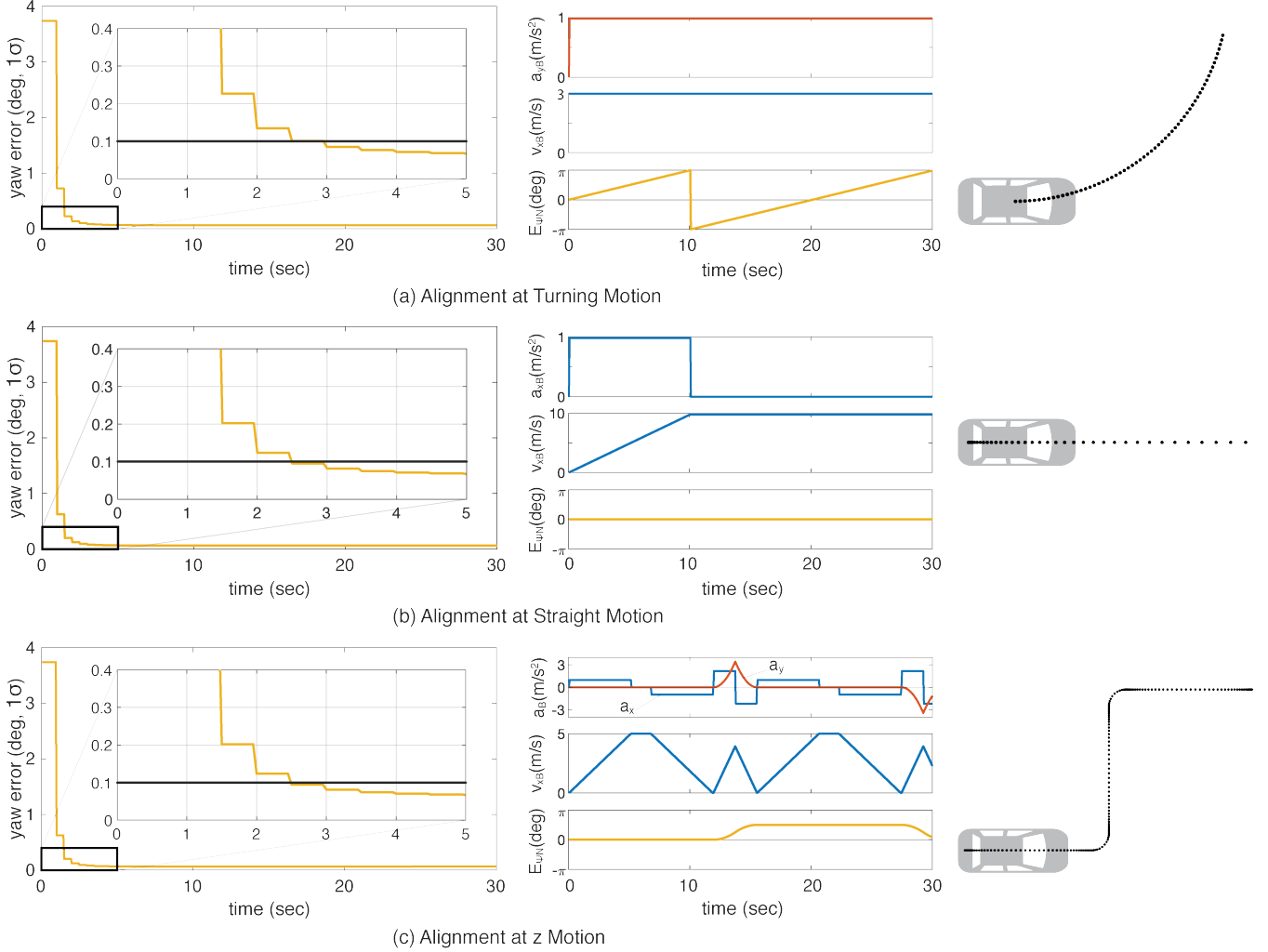


**Figure 7:** The behavior of yaw angle error when centripetal (a) or tangential (b) acceleration is applied; (c) shows the behavior while following a z-shaped path. The yaw angle can be aligned in a couple of seconds in each case.

## VI. EVALUATING INTEGRATION OF NAVIGATION SYSTEMS IN URBAN ENVIRONMENTS

After initialization and alignment in the open sky environment, we simulate the vehicle traveling into the urban core. The urban environment in our study is 3D-mapped State Street in Chicago, which runs north-south and transits from low rise neighborhoods to central downtown. We select one congested section surrounded by tall buildings and compute position error standard deviation along the path. The evaluation points are at 10 m intervals over a total distance of 170 m. The yellow lines in Fig. 8 express the visible satellites, identified by PRN numbers, at each point. We assume for convenience in the present analysis that the GPS/INS system is initialized and aligned at the first evaluation point. In reality, we would expect a degraded initial condition since we are starting the simulation in an urban canyon.

In the first simulation, the car equipped with the INS/GPS system is moving at one of two different speeds, 1 m/s or 5 m/s. The y-axis in Fig. 9 represents the position error standard deviation, and the x-axis represents the distance in meters. The dotted line expresses the number of visible satellites. The error when the vehicle velocity is 1 m/s exceeds the maximum allowable position error standard deviation,  $\sigma_{pos} = 0.1$  m, at the distance of 60 m. However, when the velocity is of 5 m/s the maximum allowable position error standard deviation is never reached. It is also clear from the figures that error propagation is significantly affected by the number of visible satellites.

In the second simulation, we compare two different navigation systems, INS/GPS and INS/GPS/WSS/VDC. The vehicle is moving at 1 m/s in the same urban environment. The INS/GPS/WSS/VDC system does provide relief, but the error propagation is still clearly affected by the number of visible satellites (Fig. 10).

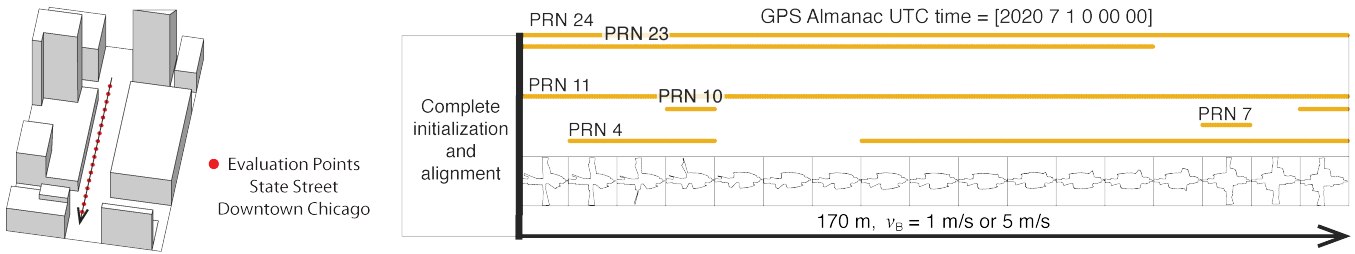


**Figure 8:** Evaluation points and PRN numbers of visible satellites at each point.

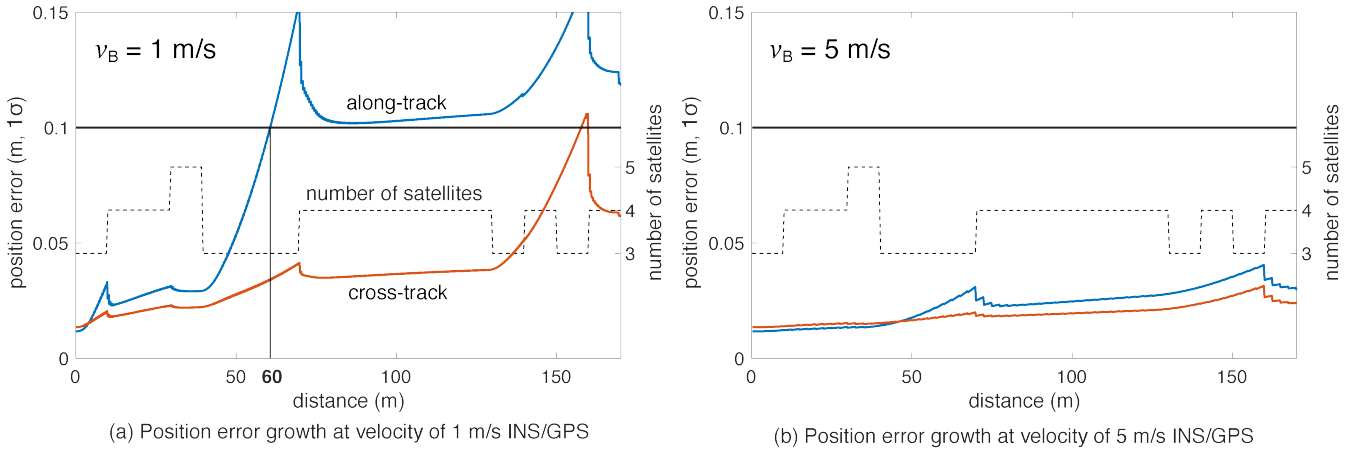


**Figure 9:** A comparison of position error growth between velocities of 1 m/s and 5 m/s.

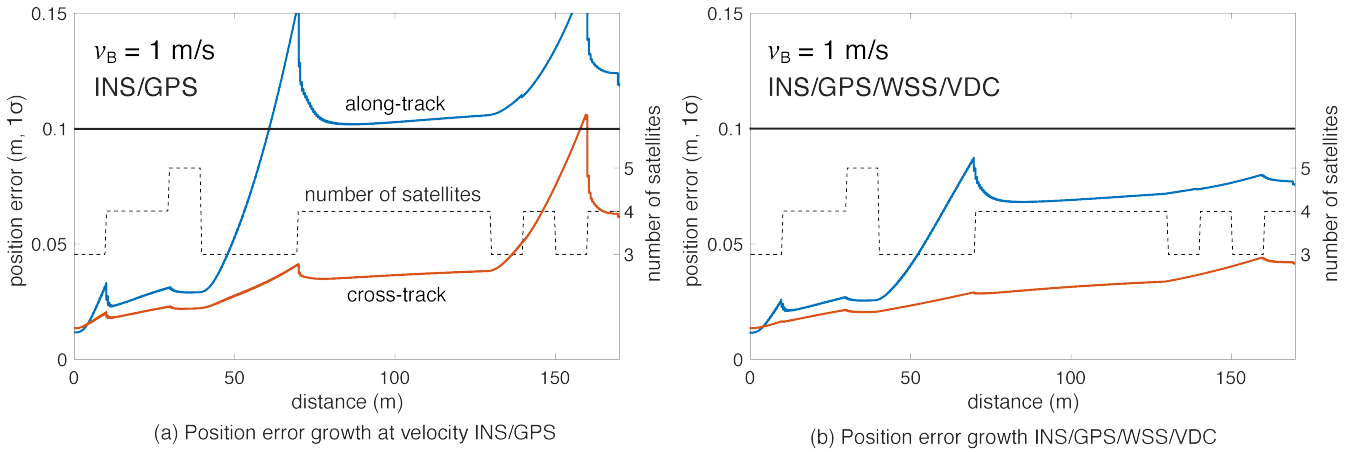


**Figure 10:** A comparison of position error growth between the INS/GPS and INS/GPS/WSS/VDC systems for 1 m/s velocity.

In GNSS-challenged environments, INS error propagation is a function of *time*. When a vehicle moves faster, it clears the blockage area more quickly, reducing the impact of INS drift, which is a function of time, not distance. In contrast GNSS error is completely determined by *emphlocation*. Because INS error propagation depends on how long the vehicle stays in an area of GNSS outage, protection levels for trips through the same area will be different if the vehicle is smoothly cruising or gets stuck in a traffic jam.

## VII. CONCLUSION

To gain a better understanding of how long and under what local conditions multi-sensor integrated navigation systems can maintain fault-free integrity, we evaluate navigation positioning errors in 3D-mapped downtown Chicago. The system we

develop consists of sensors that self-driving cars would reasonably be equipped with: GNSS, INS, wheel speed sensor, and dynamic constraints. We begin by demonstrating the initialization and alignment process wherein a self-driving car achieves targeted initial error variances. Then the performance of the integrated navigation system is evaluated for a car driving through a section of 3D-mapped downtown Chicago. We show that INS/GPS position errors along the path depend very strongly on the velocity of the vehicle. When augmented with WSS/VDC position errors are suppressed, but the error propagation is still strongly influenced by to the number of visible satellites.

## ACKNOWLEDGEMENTS

This research is supported by the National Science Foundation (Grant No. 1830642).

Fig. 1 was created by Alexis Arias, Landscape Architecture + Urbanism, IIT. The authors greatly appreciate the advice and help of Nilay Mistry, Landscape Architecture + Urbanism.

## REFERENCES

- [1] K. Nagai, T. Fasoro, M. Spenko, R. Henderson, and B. Pervan, "Evaluating GNSS navigation availability in 3-D mapped urban environments," *2020 IEEE/ION Position, Location and Navigation Symposium, PLANS 2020*, pp. 639–646, 2020.
- [2] P. D. Groves, "Shadow matching: A new GNSS positioning technique for urban canyons," *Journal of Navigation*, vol. 64, no. 3, pp. 417–430, 2011.
- [3] L. Chapman, J. E. Thornes, and A. V. Bradley, "Sky-view factor approximation using GPS receivers," *International Journal of Climatology*, vol. 22, no. 5, pp. 615–621, 2002.
- [4] A. S. Householder, "Unitary triangularization of a nonsymmetric matrix," *Journal of the ACM (JACM)*, vol. 5, no. 4, pp. 339–342, 1958.
- [5] T. G. Reid, S. E. Houts, R. Cammarata, G. Mills, S. Agarwal, A. Vora, and G. Pandey, "Localization requirements for autonomous vehicles," *SAE International Journal of Connected and Automated Vehicles*, vol. 2, no. 3, pp. 1–16, 2019.
- [6] G. Falco, M. Pini, and G. Marucco, "Loose and tight GNSS/INS integrations: comparison of performance assessed in real urban scenarios," *Sensors (Switzerland)*, vol. 17, no. 2, 2017.
- [7] J. Gao, M. G. Petovello, and M. E. Cannon, "Development of precise GPS/INS/wheel speed sensor/yaw rate sensor integrated vehicular positioning system," *Proceedings of the Institute of Navigation, National Technical Meeting*, vol. 2, no. January, pp. 780–792, 2006.
- [8] C. Tanil, "Detecting GNSS spoofing attacks using INS coupling," Ph.D. dissertation, Illinois Institute of Technology, 2016.
- [9] S. Khanafseh, B. Kujur, M. Joerger, T. Walter, S. Pullen, J. Blanch, K. Doherty, L. Norman, L. de Groot, and B. Pervan, "GNSS multipath error modeling for automotive applications," *Proceedings of the 31st International Technical Meeting of the Satellite Division of the Institute of Navigation, ION GNSS+ 2018*, pp. 1573–1589, 2018.
- [10] Y. Bar-Shalom, X. Li, and T. Kirubarajan, *Estimation with Applications to Tracking and Navigation: Theory Algorithms and Software*. Wiley, 2004.

## APPENDIX: DERIVATION OF WHEEL SPEED SENSOR AND DYNAMIC CONSTRAINT MODEL

From the geometry in the figure, the displacement vector from the origin of the navigation frame  $O$  to the rear axle center point  $A_c$  in the navigation frame  $N$  is

$${}^O\mathbf{r}^{A_c} = {}^O\mathbf{r}^S + {}^S\mathbf{r}^{A_c} \quad (7)$$

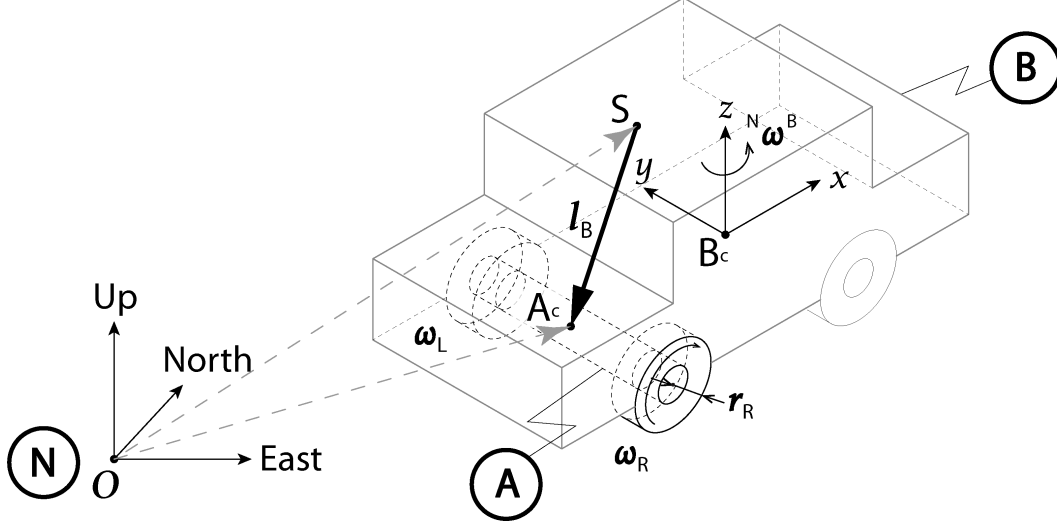
where,  $S$  is the GNSS antenna location.

The first derivative of (7) with respect to  $N$  gives the velocity

$${}^N\mathbf{v}^{A_c} = {}^N\mathbf{v}^S + {}^B\mathbf{v}^{A_c} + {}^N\boldsymbol{\omega}^B \times \mathbf{l}_B \quad (8)$$

where,

- ${}^N\boldsymbol{\omega}^B$  is the angular velocity of the body frame  $B$  relative to  $N$ ,
- $\mathbf{l}_B$  is the displacement vector from  $S$  to  $A_c$ , assumed to approximately constant in frame  $B$ .



Expressing all the elements of (8) in  $B$ -frame coordinates and the vector cross product as a skew-symmetric matrix,

$${}^N \mathbf{v}_B^{A_c} = {}^B \mathbf{R}^N \mathbf{v}_B^S + {}^B \mathbf{v}_B^{A_c} - \mathbf{L}_B {}^N \boldsymbol{\omega}_B^B \quad (9)$$

where,

- ${}^B \mathbf{v}_B^{A_c} = [0 \ 0 \ \dot{h}_s]^T$  is the shock absorber displacement,
- ${}^N \mathbf{v}_B^{A_c} = \begin{bmatrix} (\omega_R r_R + \omega_L r_L)/2 \\ 0 \\ \dot{h}_t \end{bmatrix}$  is the velocity measured by wheel speed sensors ( $\omega_{R,L}$ ) in the  $x$  direction, the non-holonomic constraint in the  $y$  direction, and the tire compression in the  $z$  direction,
- ${}^B \mathbf{R}^N$  is the rotation matrix from  $N$  to  $B$ ,
- $\mathbf{L}_B = \begin{bmatrix} l_1 \\ l_2 \\ l_3 \end{bmatrix} \times$  is the skew-symmetric matrix form of  $\mathbf{l}_B$ .

The radius of each rear wheel ( $r_{R,L}$ ) is expressed as a nominal radius ( $r_0$ ) and error ( $\delta r$ ).

$$\frac{\omega_R r_R + \omega_L r_L}{2} = \frac{(\omega_R + \omega_L)r_0 + (\omega_R \delta r_R + \omega_L \delta r_L)}{2} \quad (10)$$

The angular velocity  ${}^N \boldsymbol{\omega}_B^B$  consists of the gyro measurement ( ${}^I \boldsymbol{\omega}_B^B$ ) and the Earth rotation rate ( ${}^I \boldsymbol{\omega}_N^E$ ).

$${}^N \boldsymbol{\omega}_B^B = {}^I \boldsymbol{\omega}_B^B - {}^I \boldsymbol{\omega}_B^N = {}^I \boldsymbol{\omega}_B^B - {}^B \mathbf{R}^N {}^I \boldsymbol{\omega}_N^E. \quad (11)$$

Combining (9), (10), and (11),

$$\boldsymbol{\omega} = {}^B \mathbf{R}^N \mathbf{v}_N - \mathbf{L}_B {}^I \boldsymbol{\omega}_B^B + \mathbf{L}_B {}^B \mathbf{R}^N {}^I \boldsymbol{\omega}_N^E + \begin{bmatrix} -\frac{\omega_R}{2} \delta r_R - \frac{\omega_L}{2} \delta r_L \\ 0 \\ \dot{h}_s - \dot{h}_t \end{bmatrix} \quad (12)$$

where  $\boldsymbol{\omega} = \begin{bmatrix} (\omega_R + \omega_L)r_0/2 \\ 0 \\ 0 \end{bmatrix}$ .

Linearizing (12) and expressing the result in perturbation form, we obtain

$$\boldsymbol{\omega} - \boldsymbol{\omega}^* = {}^B \mathbf{R}^{N*} \delta \mathbf{v}_N + ({}^B \mathbf{R}^{N*} \mathbf{v}_N^* \times + \mathbf{L}_B {}^B \mathbf{R}^{N*} I \boldsymbol{\omega}_N^E \times) \delta \mathbf{E}_N - \mathbf{L}_B \delta^I \boldsymbol{\omega}_B^B + \begin{bmatrix} -\frac{\omega_R}{2} \delta r_R - \frac{\omega_L}{2} \delta r_L \\ 0 \\ \dot{h}_s - \dot{h}_t \end{bmatrix} \quad (13)$$

where \* represents the reference value of the variable, and  $\delta \mathbf{E}$  is the attitude vector consisting of the pitch ( $\delta\phi$ ), roll ( $\delta\theta$ ), and yaw ( $\delta\psi$ ) angles.

The gyro measurement equation is

$$\delta^I \boldsymbol{\omega}_B^B = \delta^I \tilde{\boldsymbol{\omega}}_B^B - \mathbf{b}_g - \boldsymbol{\nu}_g \quad (14)$$

where,

- $\delta^I \boldsymbol{\omega}_B^B$  is the true angular rate vector in the body frame,
- $\delta^I \tilde{\boldsymbol{\omega}}_B^B$  is the gyro angular rate measurements vector in the body frame,
- $\mathbf{b}_g$  is the gyro bias,
- $\boldsymbol{\nu}_g$  is the gyro white measurement noise.

The speed sensor measurement error is modelled as

$$\boldsymbol{\nu}_\omega \sim N(0, \sigma_\omega^2). \quad (15)$$

The non-holonomic constraint crosstrack movement violation error is modelled as

$$\zeta \sim N(0, \sigma_\zeta^2). \quad (16)$$

The holonomic constraint vertical movement violation is modelled as

$$h \equiv \dot{h}_s - \dot{h}_t \sim N(0, \sigma_h^2). \quad (17)$$

Combining (13)-(17), we obtain

$$\begin{aligned} \boldsymbol{\omega} - \boldsymbol{\omega}^* = & {}^B \mathbf{R}^{N*} \delta \mathbf{v}_N + ({}^B \mathbf{R}^{N*} \mathbf{v}_N^* \times + \mathbf{L}_B {}^B \mathbf{R}^{N*} I \boldsymbol{\omega}_N^E \times) \delta \mathbf{E}_N + \mathbf{L}_B \mathbf{b}_g \\ & + \begin{bmatrix} -\frac{\omega_R}{2} \delta r_R - \frac{\omega_L}{2} \delta r_L \\ 0 \\ 0 \end{bmatrix} - \mathbf{L}_B \delta^I \tilde{\boldsymbol{\omega}}_B^B + [\mathbf{L}_B \quad \mathbf{I}] \mathbf{v}_\omega \end{aligned} \quad (18)$$

where,  $\mathbf{v}_\omega = [\boldsymbol{\nu}_g \quad \boldsymbol{\nu}_\omega \quad \zeta \quad h]^T$  is the measurement noise vector.

Equation (18) includes the gyro measurement  $\delta^I \tilde{\boldsymbol{\omega}}_B^B$  which is also used by the EKF process model. Therefore, the measurement noise ( $\boldsymbol{\nu}_g$ ) and process noise are correlated, and we cannot integrate these models directly into the EKF. To resolve this issue, the process model and the noise are modified using the method described in Chapter 8 of [10].